RSC Advances

PAPER

View Article Online
View Journal | View Issue

Cite this: *RSC Adv.*, 2024, **14**, 3085

A photothermal MoS_2 decorated biomass carbon-based aerogel with a directionally aligned porous structure for mitigating heavy metal stress under seawater acidification

Fang Yu,[a] Xiangyu Cheng,[a] Juntian Xu*[b] and Qinfang Zhang *[a]

Marine animals and human are threatened by seawater acidification and metal contamination. Especially, the toxicity of copper (Cu) is expected to be boosted with seawater acidification. However, studies on the removal of Cu under seawater acidification are limited for practical applications, owing to obstacles such as instability, secondary contamination, and low adsorption efficiency. In this work, coconut shells were utilized for the synthesis of biomass carbon, which was then decorated with MoS_2. A novel porous MoS_2/carbon-based aerogel (MCA) with the synergistic effect of photothermal conversion and adsorption was constructed *via* directional freeze-drying technology. The adsorption properties of MCA were a precise match with Freundlich isotherm and pseudo-second-order kinetic models with a high correlation coefficient (R^2) of more than 0.995. Under solar illumination, the surface temperature of MCA reached up to 36.3 °C and the adsorption capacity of MCA increased to 833.8 mg g^{-1}, indicating that the remarkable thermal properties of MCA contributed to achieving high adsorption capacity. The adsorption mechanisms of MCA involved in the removal of Cu(II) ions were dominated by chemisorption rather than surface physical adsorption. Owing to its outstanding photothermal conversion performance and directionally aligned porous structure, MCA was able to remove Cu(II) species from seawater, and the adsorption ability of MCA reached 247.1 mg g^{-1} after ten adsorption cycles. MCA exhibited excellent stability to resist the complex natural environment and was easy to reuse. Overall, MCA with a series of merits, including high adsorption efficiency, excellent photothermal conversion property, and outstanding cycling stability, was confirmed to contribute to addressing heavy metal stress under seawater acidification.

Received 29th October 2023
Accepted 4th January 2024

DOI: 10.1039/d3ra07358k

rsc.li/rsc-advances

1. Introduction

Seawater is composed of more than 15% global species, and it is one of the vast ecosystems on the earth.[1,2] Owing to the anthropogenic emissions of CO_2, the adsorption of atmospheric CO_2 results in a decrease in the pH of seawater (a phenomenon termed as ocean acidification or seawater acidification).[3,4] Seawater acidification is capable of seriously affecting biological and physiological properties, such as energy metabolism, nutrient digestion, and immune responses.[5–7] More importantly, seawater acidification can lead to the speciation of metals and affect the toxicity of metals.[8] For instance, seawater acidification alters the migration and retention of heavy metals and then promotes the accumulation of metals or aggravates the influence of metals on organisms.[9] Several studies have indicated that seawater acidification can impact the physiological performance of aquatic species.[10,11] Despite an increasing number of studies being reported on seawater acidification, an effective method to solve the problem of heavy metal stress under seawater acidification is still needed.

Of the common heavy metals, copper (Cu) is mainly dominated by carbonate species, including $CuCO_3$ and $Cu(CO_3)_2^{2-}$, in seawater.[12,13] However, a decreased pH originating from seawater acidification will greatly increase the speciation of dissolved Cu and subsequently improve the toxicity of Cu towards marine organisms.[14] In addition, high Cu content in aquatic products will cause excessive Cu accumulation in the human body, which can contribute to methemoglobinemia, hemolytic anemia, or internal organ damage.[15] Particularly, the World Health Organization (WHO) has set the maximum acceptable limit of Cu(II) ion concentration in drinking water at 1.5 mg L^{-1}.[16] Generally, ion exchange, adsorption, and electrochemical methods are applied for disposing heavy metal ions.[17–19] In this view, as an eco-friendly and cost-efficient technology, adsorption technology has been widely utilized

[a]*School of Materials Science and Engineering, Yancheng Institute of Technology, Yancheng 224051, P. R. China. E-mail: qfangzhang@gmail.com*
[b]*Jiangsu Key Laboratory of Marine Bioresources and Environment, Jiangsu Ocean University, Lianyungang 222005, China. E-mail: jtxu@jou.edu.cn*

for the removal of Cu metal.[20,21] As an illustration, Zhao *et al.* devised poly(butylene adipate-*co*-terephthalate) (PBAT) microplastics for the adsorption of Cu(II), and the maximum adsorption quantity was 140.547 μg g^{-1}.[22] Truong *et al.* prepared iron oxide particles doped with biochar (Fe-BAB) and employing *Sargassum hemiphyllum* as a carbon source. Fe-BAB demonstrated a superior adsorption performance of Cu(II) ions of 105.3 mg g^{-1}, compared with other biochars.[23] Most of these adsorbents suffer from plenty of shortcomings, involving low renewability, secondary pollution, and poor adsorption efficiency. More importantly, these adsorbents are only treated with heavy metal ions in a single solution. In contrast, aerogels possess a controlled pore structure and high surface area, which offers sufficient adsorption sites for metal ions.[24] In addition, aerogels are easy to separate and recycle, which has the potential for practical applications in the complex marine environment.

Here, a novel photothermal-assisted aerogel with both a photothermal effect and excellent adsorption capacity was devised for the treatment of Cu heavy metal ions under seawater acidification. Specifically, the biomass carbon was decorated by MoS_2, and the MoS_2/C-based aerogel was constructed by directional freeze-drying technology. The MoS_2/C-based aerogel was then investigated for the removal of Cu(II) ions from the marine environment together with the illustration of the interrelated removal mechanisms. Furthermore, the main points were the influence of the photothermal effect on the removal of Cu(II) ions. The kinetics and isotherms of the adsorption process of Cu(II) ions on MCA were studied, and the effects of pH on the adsorption of Cu(II) ions for MCA were also explored. Recyclability tests of the MCA in actual seawater were carried out to assess the feasibility of real-world applications. Structural changes on MCA during the adsorption process were demonstrated to propose the adsorption mechanisms of the Cu(II) ions by MCA (Fig. 1).

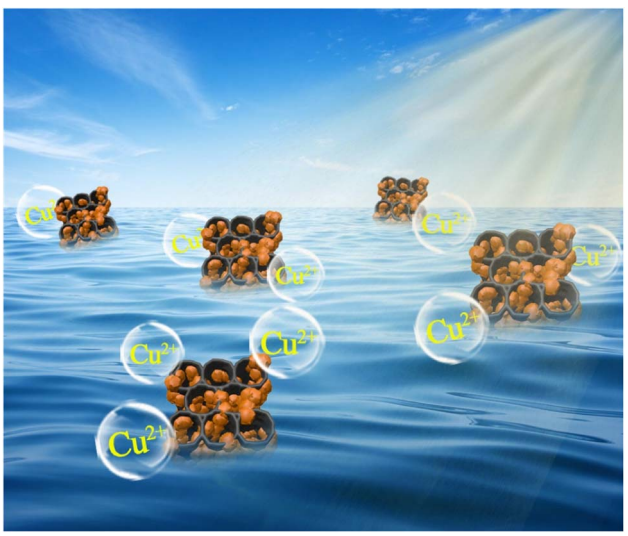

Fig. 1 Fully developed MoS_2/C-based aerogel for the application of Cu(II) heavy metal ion removal under seawater acidification.

2. Experimental section

2.1 Materials

Ammonium molybdate tetrahydrate ($(NH_4)_6Mo_7O_{24}\cdot 4H_2O$), ethanol, thiourea ($CS(NH_2)_2$), chitosan, and acetic acid were purchased from Macklin Biochemical Co., Ltd (Shanghai, China). The coconut shell was purchased from a local market. All materials in this work were used directly without any purification.

2.2 Synthesis of coconut shell-based biomass carbon

The coconut shell-based biomass carbon was prepared using a facile inert calcination method according to the literature, and the typical process was as follows.[25,26] Approximately, 1.000 g of coconut shell was soaked in 6 wt% NaOH solution, after stirring for 12 h at room temperature, it was repeatedly washed using distilled water to a pH of 7. The as-prepared coconut fiber was immersed in the $NaOH/H_2O_2$ mixture for bleaching, and heated to 80 °C for 30 min. After the completion of the reaction, the solution was cooled and the coconut fiber was washed repeatedly with distilled water. The products were then dried at 60 °C for 12 h. Finally, the coconut fiber was carbonized at 700 °C for 2 h in an Ar atmosphere, and the coconut fiber-based biomass carbon was obtained.

2.3 Synthesis of MoS_2/C-based aerogel (MCA)

MoS_2/C composites were fabricated using a one-step hydrothermal process.[27,28] Specifically, 2.4718 g of ($(NH_4)_6Mo_7O_{24}\cdot 4H_2O$), 2.1316 g of $CS(NH_2)_2$, and 0.0800 g of coconut fiber-based biomass carbon were dissolved in an 80 mL of deionized water and stirred for 30 min. The precursor solution was transferred into a 100 mL autoclave, and heated at 200 °C for 18 h. The resulting precipitate was centrifuged and washed three times using deionized water and ethanol. Then, the product was dried in an oven at 60 °C overnight. The MCA was obtained by directional freeze-drying technology. The chitosan was dissolved in an aqueous acetic acid solution, and heated at 80 °C to form a uniform solution. MCA were added into the above chitosan solution, and mechanically stirred for 1 h. Then, the aqueous dispersion was placed in a cylindrical mold, and liquid nitrogen was added for pre-cooling. The mold was transferred to a vacuum freeze dryer at −60 °C for 48 h, and then the directional MCA was obtained. For comparison, the biomass carbon-based aerogel (CA) was also prepared by the same methodology.

2.4 Characterization

X-ray diffraction (XRD) patterns obtained on a Bruker Advance D8 diffractometer by Cu Kα radiation at 40 kV and 200 mA were utilized to investigate the crystal structure. The microscopic morphology of samples was examined by field-emission scanning electron microscopy (FESEM, JSM7100F, Japan). The microstructure of the samples was studied using a field emission transmission electron microscope (FETEM, JEM-2100F, Japan), coupled with an energy dispersive X-ray spectrometer

(EDX) to study the elemental distribution. X-ray photoelectron spectroscopy (XPS, ESCALAB 250Xi, ThermoFisher Scientific, America) was performed to validate the surface elements of samples. A universal testing machine (CLY2768TM-10, USA) was used to test the mechanical strength of the sample. The thermal conductivity (λ) of the sample was obtained using the following formula:

$$q = \frac{\lambda \mathrm{d}T}{\mathrm{d}x} \quad (1)$$

where q is the heat flux, dT is the temperature difference, and dx refers to the distance difference.

The thermal resistance (R) was calculated using the equation:

$$R = \frac{d}{\lambda} \quad (2)$$

where λ is the thermal conductivity of the MCA, and d is the thickness.

2.5 Adsorption experiment

A series of Cu(II) (Cu^{2+}) solutions at different concentrations ranging from 5 to 200 mg L^{-1} were used to explore the adsorption effect of MCA and biomass carbon-based aerogel on Cu^{2+}. The effects of pH (1, 2, 3, 4, 5, and 6) and time (10, 20, 30, 50, 60, 120, and 150 min) on the adsorption of Cu^{2+} by MCA and CA were also explored. All adsorption experiments were carried out in a constant temperature incubator shaker at 25 °C for 12 h. The supernatant was obtained using a needle-type water filter, and the Cu^{2+} concentrations were measured using a copper low-range portable photometer (HI96747, resolution of 0.001 mg L^{-1}, Hanna Instruments). The adsorption isotherm experiments were conducted on MCA to further explore the adsorption mechanism.

The adsorption capacities (q_e) of Cu^{2+} on MAC and CA were calculated using the following formula:[29]

$$q_e = \frac{(c_t - c_0)}{m} \times v \quad (3)$$

where c_t (mg L^{-1}) is the final concentration of Cu^{2+}, c_0 (mg L^{-1}) is the initial concentration of Cu^{2+}, m (g) is the mass of the adsorbent, and v (mL) is the volume of the solution.

2.6 Adsorption isotherms and kinetics

For the adsorption isotherm experiments, 0.0200 g MAC and CA were immersed in 100 mL of Cu(II) solution at different initial concentrations, and shaken at 180 rpm in the dark at 25 °C, 35 °C, and 45 °C for 12 h, respectively. The obtained data was

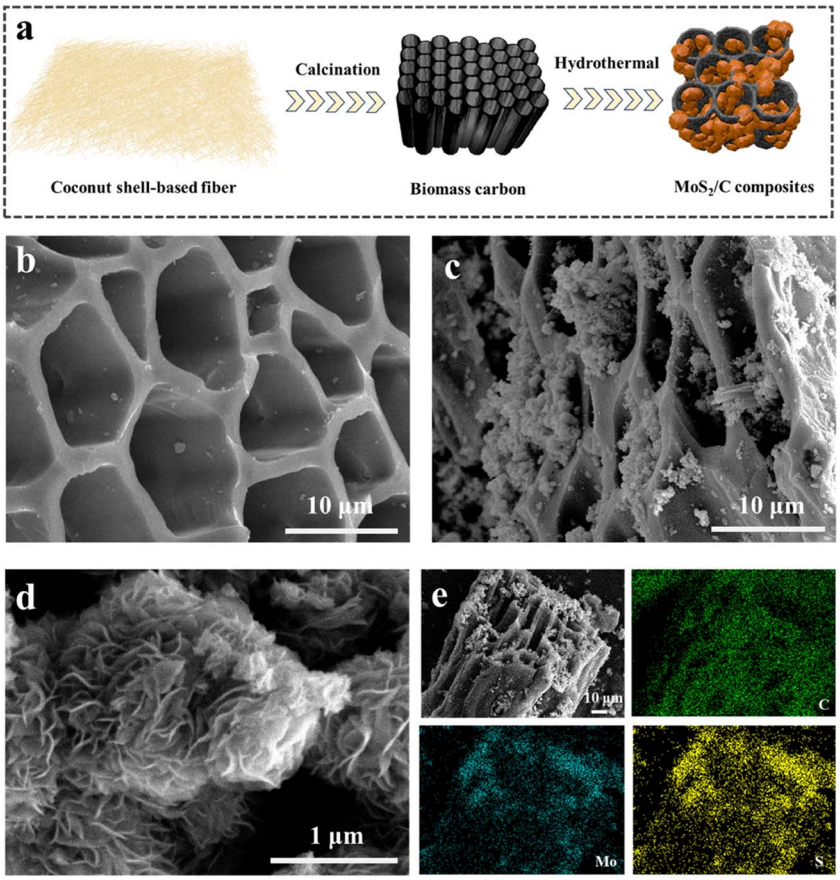

Fig. 2 (a) Schematic illustration for preparing MoS_2/C composites for Cu(II) ion removal; SEM images of (b) coconut shell-based biomass carbon and (c) and (d) MoS_2/C composites; (e) elemental mapping images of Mo, S, and C in MoS_2/C composites.

assessed using the Langmuir and Freundlich isotherm models:[30,31]

$$\frac{C_e}{q_e} = \frac{C_e}{q_m} + \frac{1}{K_L q_m} \quad (4)$$

$$\ln q_e = \ln K_F + \frac{1}{n} \ln C_e \quad (5)$$

where q_e (mg g^{-1}) is the equilibrium adsorption ability; q_m (mg g^{-1}) represents the maximum adsorption capacity of the adsorbents at the monolayer; K_F (L mg^{-1}) and K_L are the equilibrium constants of the Langmuir and Freundlich isotherm models, respectively; n (mg g^{-1}) is an empirical coefficient for Freundlich isotherm models in connection with the adsorption capacity.

Adsorption kinetic experiments of MAC and CA at different adsorption times were conducted to give valuable evidence for the reaction pathways and the possible adsorption mechanisms. The adsorption experiments were performed at 25 °C with a pH of 6.0, and the data was described using the pseudo-first-order and pseudo-second-order models. The calculation formulas of the model are as follows:[32,33]

$$\ln q_e - \ln q_t = \ln q_e - k_1 t \quad (6)$$

$$\frac{t}{q_t} = \frac{1}{k_2 q_e^2} + \frac{t}{q_e} \quad (7)$$

where k_1 (min^{-1}) and k_2 (g mg^{-1} min^{-1}) are the rate constants of the pseudo-first-order and pseudo-second-order models, respectively; q_t (mg g^{-1}) is the adsorption capacity of the absorbents at different times.

2.7 Photothermal conversion properties

A solar simulator (CEL-S500, Zhongjiaojinyuan, Beijing) equipped with an optical filter for the standard AM 1.5G spectrum was used as a solar source. The samples were illuminated under one sun intensity (1 kW m^{-2}). The temperature of the samples was tested using an IR camera (FLIR E4 Pro, America) and K-type thermocouples.

3. Results and discussion

The schematic of the fabrication of MoS_2/C composites is presented in Fig. 2a. The coconut shell-based biomass carbon was employed as the substrate for the growth of MoS_2, and the MoS_2 nanoflower grew on the surface of the coconut shell-based fiber *via* a facile hydrothermal reaction. As depicted in Fig. 2b, the FESEM image for the coconut shell-based fiber presented a general view and indicated that the fiber exhibited a porous hollow-tube structure with smooth walls. The unique structure of the coconut shell-based fiber not only was beneficial to MoS_2 nanosheets *via in situ* fabrication, but also could facilitate mass transfer and ion adsorption. Compared with the carbon fiber, the MoS_2/C composites showed flower-like coating layers, which were generated by the self-assembly of MoS_2 nanosheets (Fig. 2c and d). The elemental distribution of MoS_2/C composites, shown in Fig. 2e, suggested the uniform distribution of Mo, S, and C elements. In addition, the high-resolution transmission electron microscopy (HRTEM) images of the MoS_2/C composites, shown in Fig. 3a and b, illustrated that the MoS_2 nanoflower was clearly observed on the surface. The interlayer

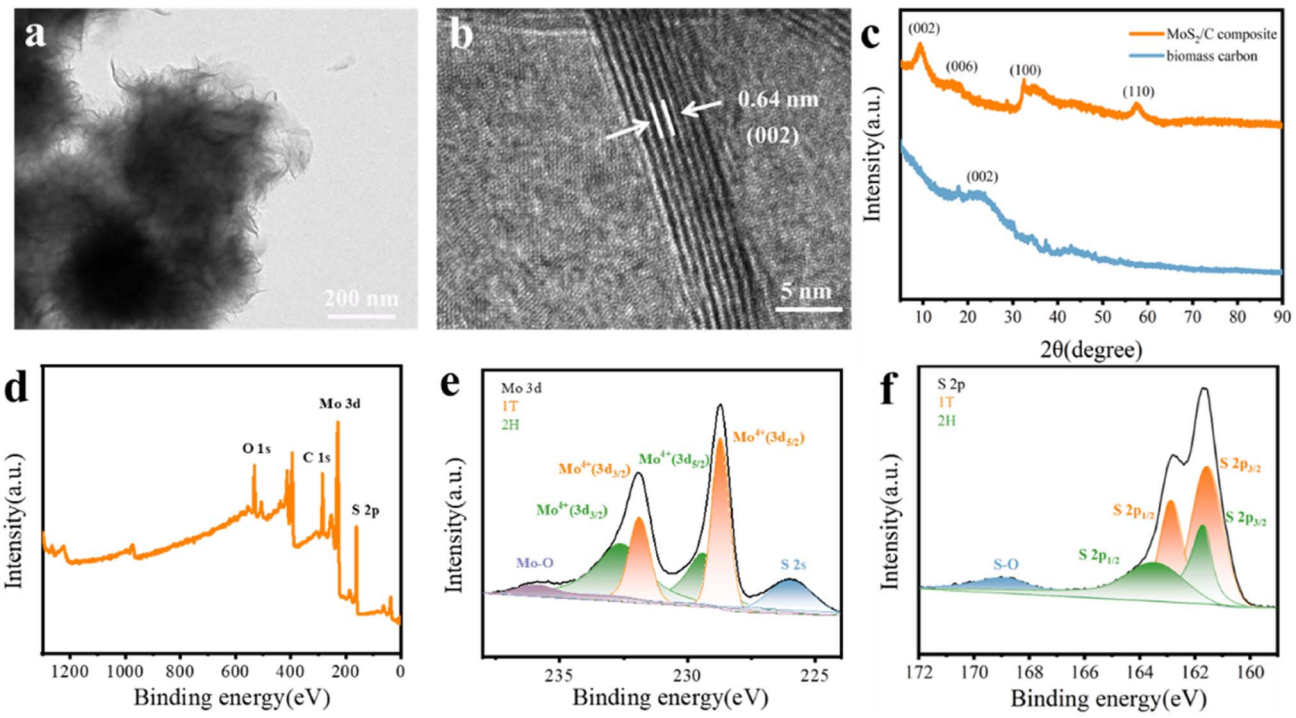

Fig. 3 (a) and (b) TEM and HRTEM images of MoS_2/C composites; (c) XRD patterns of the coconut shell-based biomass carbon and MoS_2/C composites; (d) survey XPS spectrum of MoS_2/C composites; (e) Mo 3d, and (f) S 2p XPS spectra of MoS_2/C composites.

spacing was 0.64 nm, corresponding to the (002) crystal plane of MoS_2, which was larger than the standard lattice value of MoS_2 (0.615 nm) reported in the previous literature.[34,35]

The crystal structure and phase composition of the coconut fiber-based biomass carbon and MoS_2/C composites were characterized by X-ray diffraction (XRD), as depicted in Fig. 3c. The as-prepared coconut fiber-based biomass carbon possessed a distinct carbon-specific peak at 23.4°, manifesting the (002) plane of the graphite-like structure.[36] The characteristic peaks of MoS_2/C composites at 9.4°, 15.3°, 32.5°, and 57.5° were assigned to (002), (006), (100), and (110) planes, respectively.[37] The diffraction peak of (002) of MoS_2/C composites shifted to a lower scattering angle of 9.4°, which was ascribed to 1T-MoS_2.[38] The characteristic peak at (002) of the MoS_2/C composites was very sharp, MoS_2 possessed an excellent crystallinity, as previously proved by a similar result of HRTEM. The phase conversion was ascribed to the insertion of NH^{4+} and CO_2. The insertion extended the interlayer distance, resulting in a distortion in the 2H phase structure.[39] X-ray photoelectron spectroscopy (XPS) was conducted for the investigation of the chemical state of elements of MoS_2/C composites. The survey XPS spectrum of MoS_2/C composites showed Mo, S, C, N, and O elements, suggesting the existence of biomass and MoS_2 (Fig. 3d). The high-resolution of XPS spectrum of Mo 3d demonstrated the existence of hybridized 1T/2H phases in the MoS_2/C composites (Fig. 3e). The couple prevalent peaks at 228.7 and 231.9 eV were attributed to Mo $3d_{5/2}$ and Mo $3d_{3/2}$, respectively, of the 1T phase MoS_2.[40] While the other two doublets centered at 229.4 eV and 232.6 eV were assigned to the 2H phase.[41] The concentration of the 1T phase was calculated to be approximately 60.1%. For the S 2p high-resolution spectrum, the pair of the strong peaks located at 161.5 and 162.8 eV corresponded to S $2p_{3/2}$ and S $2p_{1/2}$ of the 1T phase MoS_2 in MoS_2/C composites.[42] Simultaneously, the two peaks at 161.7 and 163.4 eV are attributed to S $2p_{3/2}$ and S $2p_{1/2}$, respectively, of the 2H phase (Fig. 3f). In addition, the C 1s spectrum in Fig. 4a was deconvoluted into two peaks at 284.6, and 285.4 eV, indicating the existence of C–C bond, and C–O bond, respectively.[43] The O 1s spectrum is presented in Fig. 4b; the peaks at 530.5, 531.7, and 533.5 eV belong to C═O, C–O–Mo and C–OH bonds, respectively.[44] The XPS spectrum of N 1s displayed four peaks, as shown in Fig. 4c, and are assigned to the Mo–N bond, pyridinic N, pyrrolic N, and graphitic N, respectively.[45]

The porous structure of the aerogels has a direct impact on controlling the flow of water and the exposure of active sites, and the aerogel that MCA was conducted by MoS_2/C composites and chitosan. The microstructure and morphologies of the MCA were studied by FESEM, as shown in Fig. 4d. MCA presented a three-dimensional and vertically aligned structure, which was similar to the CA without the addition of MoS_2/C composites. The vertically aligned porous structure was likely to have more ice-ordered growth during the freezing process.[46] Moreover, the average width of the vertically aligned pores was about 15 μm, and the average wall thickness was 2 μm. As shown in Fig. 4e, Mo, S, C, N, and O elements were evenly distributed on the entire MCA, demonstrating the co-existence of all components in the MCA aerogel network. The mechanical strength of the MCA was measured, and the stress test data of MCA from 0 to 60% strain is shown in Fig. 4f. The three deformation regions included a relative flat elastic deformation at the initial stage, fast deformation, and the final completely buckling stage. The compressive strength of MCA was as high as 244.5 MPa at 60%

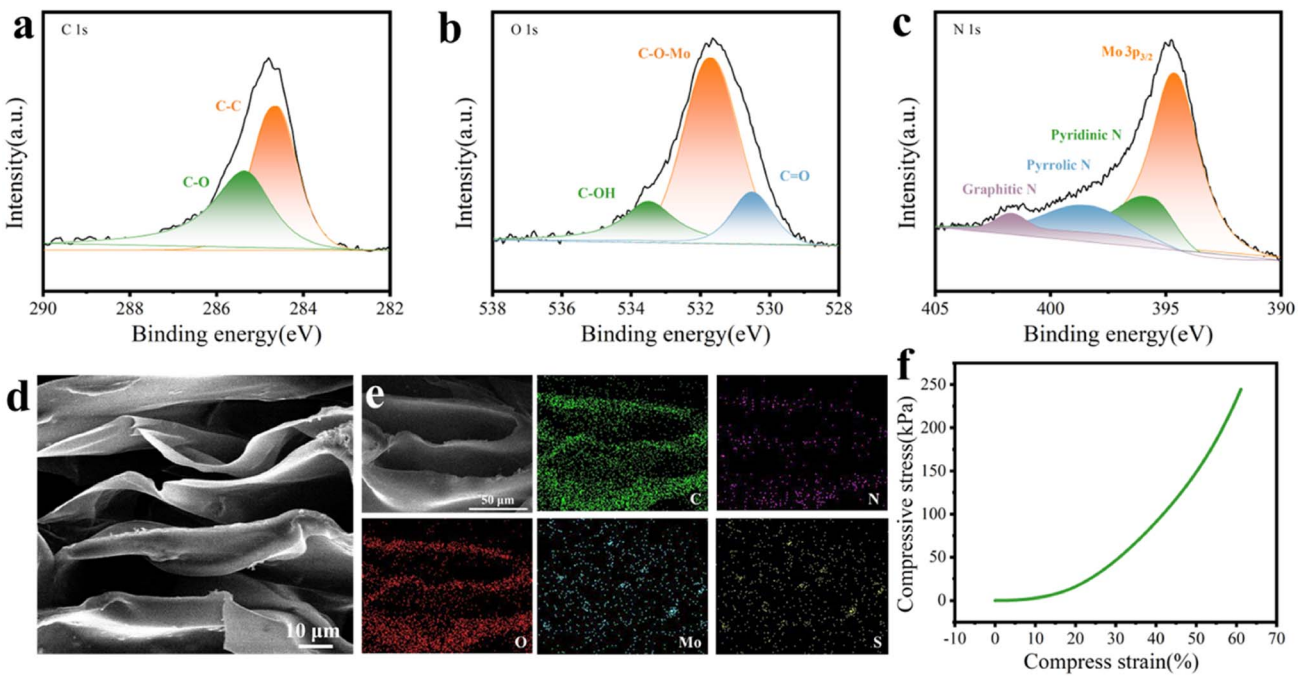

Fig. 4 (a) C 1s, (b) O 1s, and (c) N 1s XPS spectra of MoS_2/C composites; (d) SEM images of MCA showing a vertical channel structure; (e) EDS mappings images of Mo, S, C, N, and O elements in MCA; (f) strain–stress curve of the compressive test of MCA.

compressive strain, indicating that MCA exhibited excellent remarkable mechanical stability.

The different initial concentrations (5, 10, 20, 50, 100, 150, and 200 mg L^{-1}) of Cu(II) solution were selected to explore the effect of temperature on the adsorption behavior. The isotherm curves are demonstrated in Fig. 5a–d, and the relevant isotherm parameters originating from the Langmuir and Freundlich isotherm models as well as determination coefficients (R^2) are listed in Table 1. Compared with the Langmuir model, the Freundlich model was able to express the adsorption process of the MCA and CA for Cu(II) ions with relatively higher R_2 values. Cu(II) ion adsorption on MCA and CA followed the form of a multilayer occurring on the surface of the MoS_2/C composites and biomass carbon with active adsorption sites by chemical processes through the sharing or exchange of electrons.[47] The maximum adsorption capacities of MCA and CA for Cu(II) ions from the Langmuir isotherm models were 947.5 and 937.3 mg g^{-1} at 45 °C, respectively. More importantly, the adsorption ability of MCA for Cu(II) ions was higher than that for other adsorbents reported in the literature, as displayed in Table 2.[48–53]

Moreover, the adsorption capacities of MCA and CA were higher at higher temperatures, implying the increasing temperature of the adsorption process seemed to be beneficial for adsorptive abilities. One benefit of choosing MCA was its outstanding photothermal conversion ability, which was conducive to promoting the adsorption of Cu(II) ions. MCA was added to a Cu(II) ions solution with different concentrations to investigate the photothermal heating effect. The photothermal

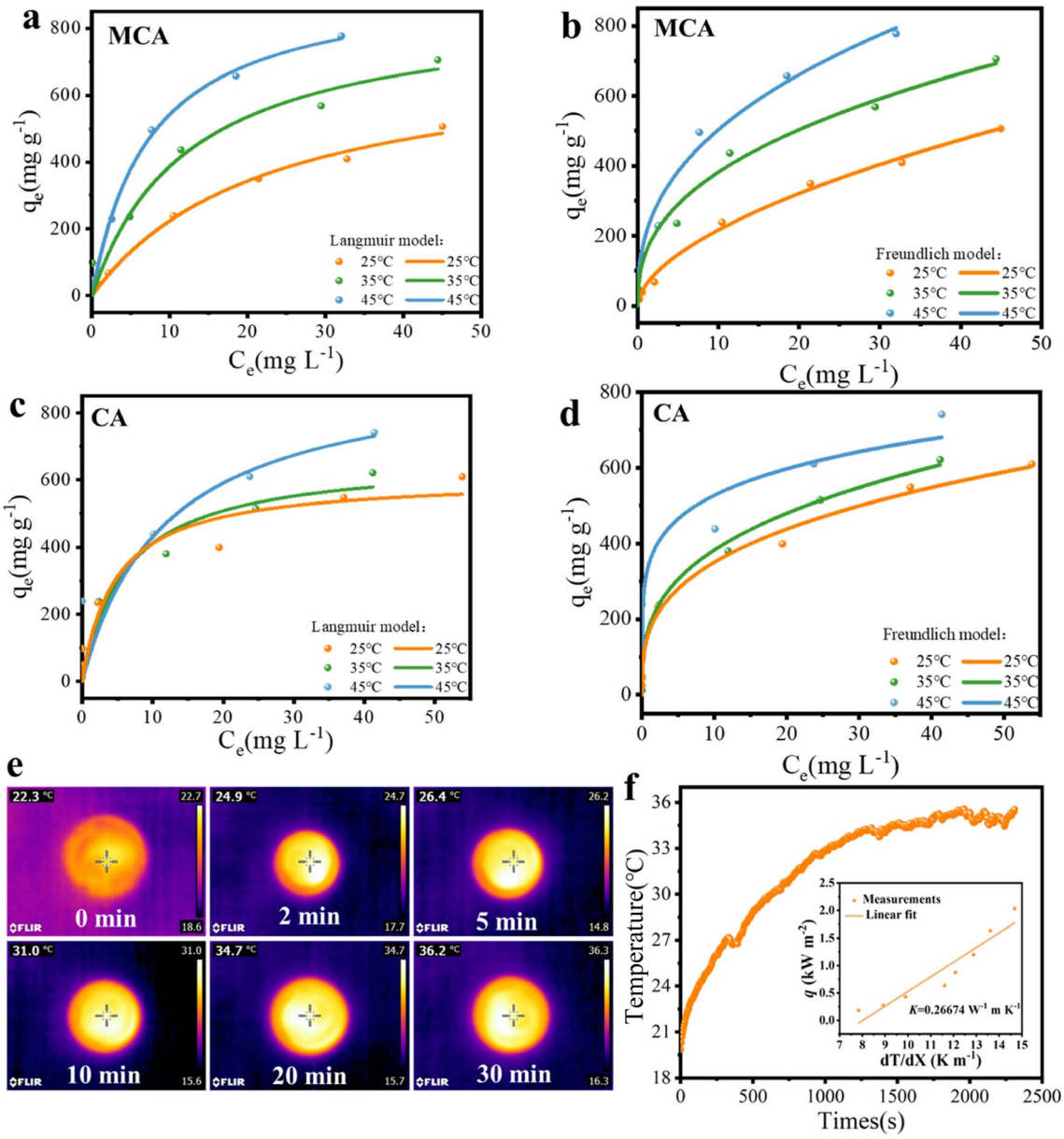

Fig. 5 (a)–(d) Adsorption isotherms of MCA and CA for Cu(II) removal at different temperatures; (e) and (f) temporal changes in the surface temperature of MCA under solar illumination and the inset image showing the thermal conductivity of MCA.

Table 1 Isotherm parameters for the adsorption of Cu(II) ions by MCA and CA at different temperatures

		Langmuir model			Freundlich model		
Adsorbent	Temperature (°C)	q_{max}/(mg g^{-1})	n	R^2	K_f/(L mg^{-1})	n	R^2
MCA	25	729.98048	0.04441	0.9928	59.11562	1.77057	0.9946
	35	867.42244	0.08068	0.96715	152.32472	2.50563	0.98409
	45	947.47883	0.13427	0.97898	204.39097	2.55382	0.98057
CA	25	606.04337	0.21098	0.92925	166.82647	3.10254	0.95939
	35	665.11685	0.16196	0.94467	180.7074	3.06755	0.99361
	45	937.30764	0.08512	0.86124	348.41519	5.56313	0.94638

conversion performance was directly related to the local temperature, the surface temperature of a Cu(II) ion solution (50 mg L^{-1}) under one sun illumination was tested. As presented in Fig. 5e and f, the temperature of the Cu(II) ion solution increased only slightly, and MCA was more responsive to temperature. The surface temperature of the MCA rose from 22.7 °C to 36.3 °C. The temperature change curve indicated that the MCA exhibited excellent photothermal effects, the MCA was able to convert the solar energy into thermal energy more quickly and efficiently. Furthermore, the thermal resistance (R)

Table 2 The theoretical maximum adsorption capacity of various adsorbents for Cu(II) ions

Adsorbent	q_{max}/(mg g^{-1})	Temperature (°C)	References
Fe_3O_4@carbon@Z1F-8	226.24	25	48
MCs@Mg/Fe-LDHs	338.98	60	49
E-CS aerogel	108.14	25	50
Magnetic biosorbent	90.00	—	51
Enhanced nano-hydroxyapatite	272.00	25	52
C-Phenylcalix[4]pyrogallolarene	8.14	25	53
MCA	730.1	25	This work

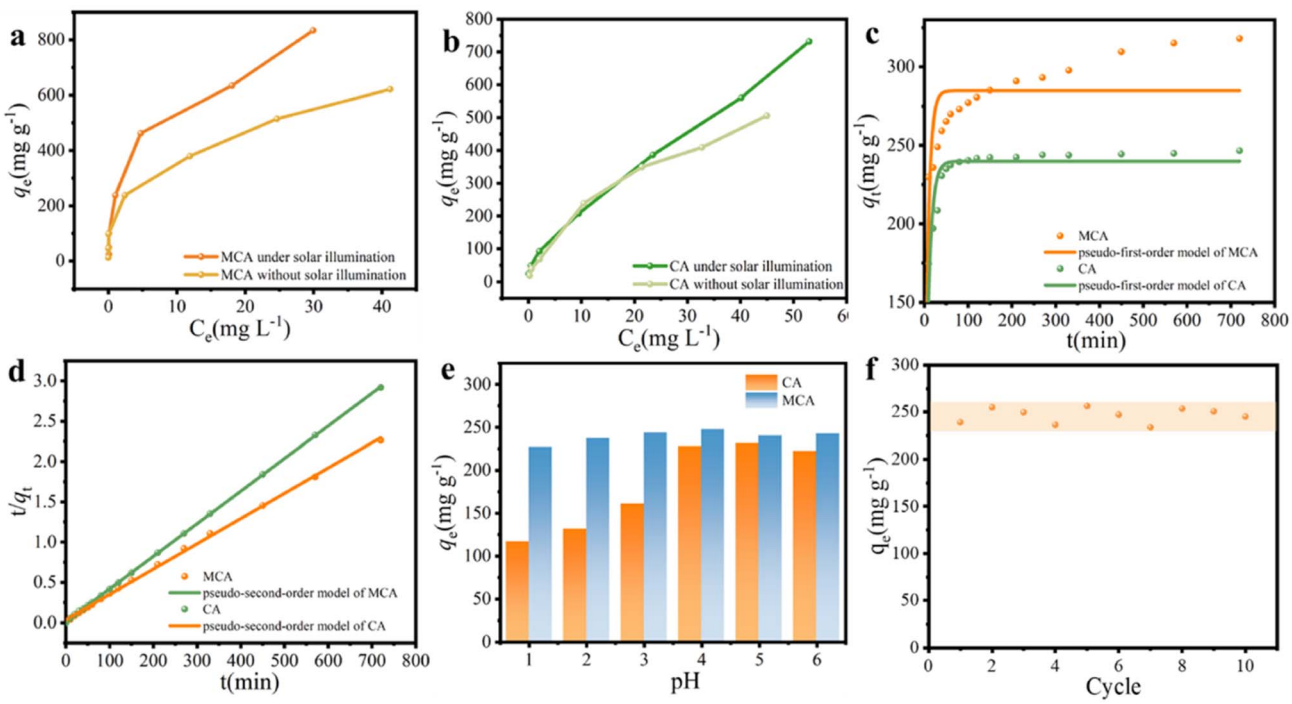

Fig. 6 (a) and (b) The influence of the photothermal effect on the adsorption capacity of MCA and CA; (c) and (d) adsorption kinetic curves of MCA and CA; (e) the effect of pH at 1.0–6.0 on the adsorption capacity of MCA and CA; (f) reusability experiments of MCA for the adsorption of Cu(II) ions in seawater with an initial pH of 4.

Table 3 Kinetic parameters for the adsorption of Cu(II) ions by MCA and CA at 25 °C

	Pseudo-first-order kinetic model			Pseudo-second-order kinetic model		
Adsorbent	q_e/(mg g^{-1})	K_1/(min^{-1})	R^2	q_e/(mg g^{-1})	K_2/(g mg^{-1} min^{-1})	R^2
MCA	284.74627	0.12745	0.92238	318.4713	0.00027	0.99912
CA	239.8689	0.10515	0.97955	246.9136	0.00126	0.99995

of the MCA was also explored. The thermal conductivity of MCA was operated at 0.26674 W m^{-1} K^{-1} as displayed in the inset image. MCA possessed a low thermal resistance of 299.9 cm^2 K W^{-1}, which was conducive to preventing the thermal energy from dissipating. Under solar illumination, the increased solution temperatures resulted in faster diffusion rates of Cu(II) ions and more Cu(II) ions were able to contact the MCA, which benefited the adsorption rates. The adsorption capacity of MCA increased to 833.8 mg g^{-1}, while that of the CA was 731.6 mg g^{-1}, under solar illumination (Fig. 6a and b). Therefore, the remarkable thermal properties of MCA were also very significant for achieving high adsorption capacity.

The adsorption rate and the dominant factors of Cu(II) ions on MCA and CA were investigated using adsorption kinetics. In general, Cu(II) ions absorbed by MCA and CA were fast at the initial stage and subsequently became slow. As shown in Fig. 6c and d, the rapid uptake stage of an amount of Cu(II) ions was at the first 50 min, after which the adsorption rate showed a declining trend. With time, the adsorption capacity reached the equilibrium, owing to the decrease of available active adsorption sites. Thus, pseudo-first-order and pseudo-second-order kinetic models were adopted to further probe the adsorption mechanism of the MCA and CA for Cu(II) ions as well as the controlled step of the solid–liquid systems. The calculated kinetic parameters are summarized in Table 3. The R^2 values of the pseudo-second-order model for MCA and CA were 0.999, and 0.999, respectively, all of which were slightly greater than the pseudo-first-order model. The pseudo-second-order kinetic model was well-matched with the adsorption behavior of MCA and CA for Cu(II) ions. From this, the rate-limiting step of Cu(II) ions adsorption on MCA and CA was chemical adsorption, which was attributed to complexation and ion exchange interaction.[54]

The influence of pH level on the adsorption performance of MCA and CA toward Cu(II) ions was studied to verify the practical application of MCA under the circumstance of seawater acidification. As displayed in Fig. 6e, the adsorption capacity of Cu(II) ions was found to be inferior at pH = 2, which was

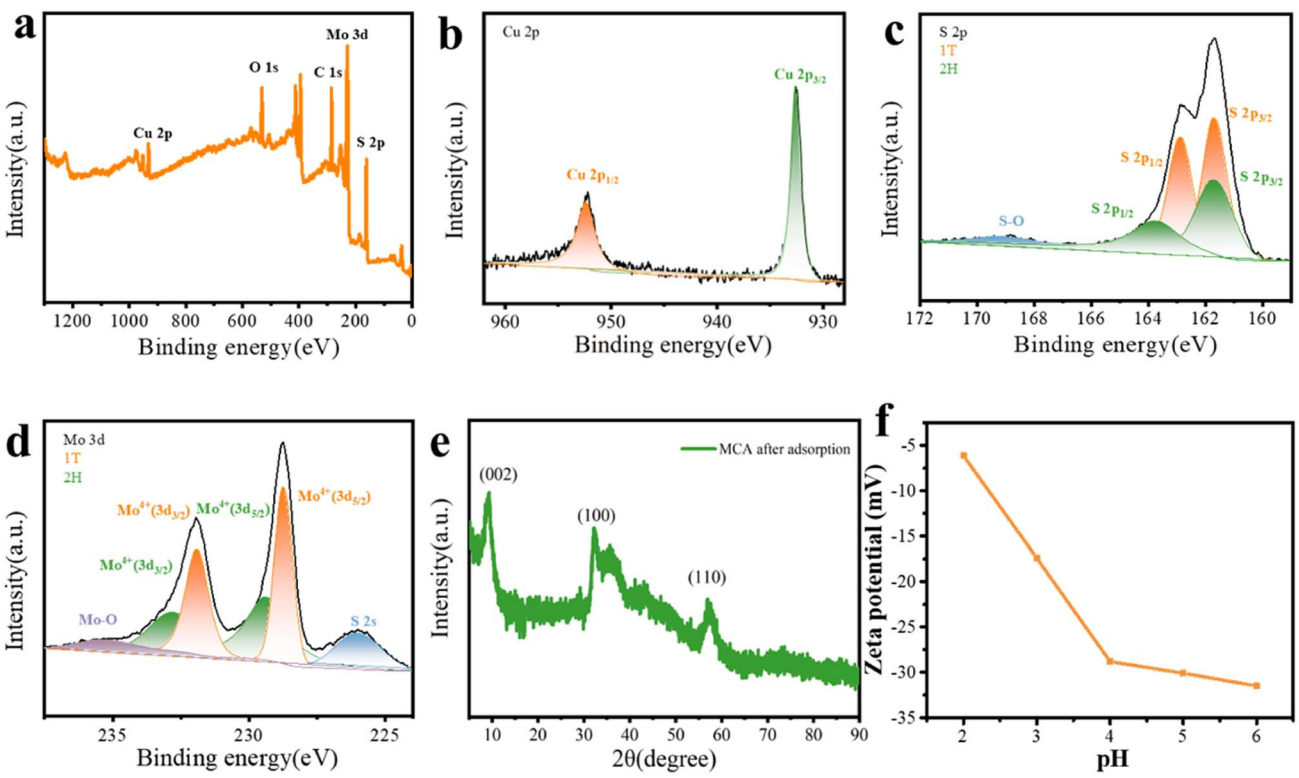

Fig. 7 (a) XPS survey, (b)–(d) high-resolution spectra for Cu 2p, S 2p, and Mo 3d of MCA after the adsorption of Cu(II) ions; (e) XRD pattern of MCA after the adsorption of Cu(II) ions; (f) zeta potential of MCA.

ascribed to the existence of the high concentration of H^+ for competing with the adsorption sites.[55] As the pH value rose from 3.0 to 6.0, the Cu(II) adsorption capacity increased slightly, and the maximum Cu(II) adsorption capacity was 247.5 mg g^{-1} at 25 °C. With the increase of pH, the electrostatic repulsion between Cu(II) ions and the surface charge of MCA decreased, resulting in the few competitive H^+ ions.[56] Seawater was employed as the water source to investigate the reusability of MCA through consecutive adsorption cycles at pH = 4. As illustrated in Fig. 6f, the adsorption capability of MCA for Cu(II) ions remained at about 247.1 mg g^{-1} after ten adsorption cycles owing to the functional groups on the surface and the directionally aligned porous structure of MCA for the efficient function of Cu(II) ion adsorption. Overall, the excellent reusability of MCA is potentially attractive for mitigating heavy metal stress under seawater acidification.

To investigate the potential adsorption mechanism of Cu(II) ions by MCA, MCA after adsorption was analyzed by XPS. The survey spectra shown in Fig. 7a exhibited obvious peaks corresponding to C 1s, O 1s, Mo 3d, S 2p, and Cu 2p. The Cu 2p spectrum showed peaks at 932.6 and 952.4 eV, which are the satellite peaks of Cu $2p_{3/2}$ and Cu $2p_{1/2}$, respectively, confirming the successful adsorption of Cu(II) cations by MCA (Fig. 7b).[57] The peaks of S 2p for 1T-MoS_2 shifted to higher binding energies at 163.1 and 161.9 eV, suggesting that the S atom was the active adsorption site (Fig. 7c).[58] As presented in Fig. 7d, with respect to Mo 3d peaks, two peaks at 228.7 and 231.9 eV belonged to the 1T-MoS_2. Simultaneously, 1T-MoS_2 possessed high stability under an ambient environment during the hydrothermal treatment, as observed from the XRD results of the MCA after its use for Cu(II) ions adsorption (Fig. 7e). In addition, the surface of MCA presented negative charges in the pH range from 2 to 6, as displayed in Fig. 7f. The enhanced adsorption capability was ascribed to the electrostatic interaction between MCA and Cu(II) ions. More importantly, owing to the metallic phase of 1T-MoS_2, electrons were more easily transferred, and 1T-MoS_2 had ultrafast adsorption kinetics compared with 2H-MoS_2.[59] Thus, the mechanism of adsorption toward Cu(II) ions by MCA was mainly attributed to chemisorption.

4. Conclusions

In summary, the novel MoS_2/carbon-based aerogel was synthesized *via* a directional freeze-drying technology, which was utilized for the removal of Cu(II) ions under seawater acidification. MoS_2/carbon-based aerogel exhibited outstanding adsorption performance for Cu(II) ions with the maximum adsorption capacity of 947.5 mg g^{-1} at 45 °C, as obtained from the Langmuir model. The adsorption process of MoS_2/carbon-based aerogel for Cu(II) ions was well described by the pseudo-second-order kinetic model and Freundlich isotherm model with a high correlation coefficient (R^2) of more than 0.995. More importantly, the surface temperature of the MCA could reach 36.3 °C under one sun illumination. The best self-heating photothermal effect of MoS_2/carbon-based aerogel was able to promote the adsorption performance, and the adsorption capacity of MCA increased to 833.8 mg g^{-1}. The mechanism of sorption was explored, and the Cu(II) ion adsorption of MoS_2/carbon-based aerogel was predominantly governed by chemisorption. The ultrafast electron transfer and electrostatic interaction between Cu(II) ions and MCA promoted the adsorption capacity of MCA. In addition, the adsorption performance of MCA was slightly affected by the acidity of the seawater. The adsorption capacity of Cu(II) ions for MoS_2/carbon-based aerogel reached 247.1 mg g^{-1} after ten adsorption cycles under seawater acidification. Therefore, MoS_2/carbon-based aerogel as a cost-effective and environmentally friendly adsorbent is expected to be applied for mitigating heavy metal stress under seawater acidification.

Author contributions

Fang Yu: writing-original draft, data curation, formal analysis, funding acquisition; Xiangyu Cheng: methodology, data curation, formal analysis; Juntian Xu: investigation; Qinfang Zhang: writing-review and editing, funding acquisition.

Conflicts of interest

There are no conflicts to declare.

Acknowledgements

The study was financially supported by the National Natural Science Foundation of China (No. 12274361), the Natural Science Foundation of Jiangsu Province (No. BK20211361), the College Natural Science Research Project of Jiangsu Province (No. 20KJA430004), the Natural Science Foundation of Jiangsu Province (No. BX2021054), and the Funding for school-level research projects of Yancheng Institute of Technology (No. xjr2021040 and No. xjr2021058).

References

1 S. Sunagawa, S. G. Acinas, P. Bork, C. Bowler, D. Eveillard, G. Gorsky, L. Guidi, D. Iudicone, E. Karsenti, F. Lombard, H. Ogata, S. Pesant, M. B. Sullivan, P. Wincker and C. Vargas, *Nat. Rev. Microbiol.*, 2020, **18**, 428–445.
2 S. H. Thangal, M. Nivetha, C. Muttharasi, K. Anandhan and T. Muralisanka, *Mar. Pollut. Bull.*, 2021, **169**, 112476.
3 D. Qi, Z. X. Ouyang, L. Q. Chen, Y. X. Wu, R. B. Lei, B. S. Chen, R. A. Feely, L. G. Anderson, W. L. Zhong, H. M. Lin, A. Polukhin, Y. X. Zhang, Y. L. Zhang, H. B. Bi, X. Y. Lin, Y. M. Luo, Y. P. Zhuang, J. F. He, J. F. Chen and W. J. Ca, *Science*, 2022, **377**, 1544–1550.
4 R. Freitasa, L. D. Marchia, M. Bastosa, A. Moreiraa, C. Velezа, S. Chiesaa, F. J. Wronab, E. Figueiraa and A. M. V. M. Soares, *Ecol. Indic.*, 2017, **79**, 54–62.
5 R. Freitas, L. Marchi, A. Moreira, J. L. T. Pestana, F. J. Wrona, E. Figueira and A. M. V. M. Soares, *Sci. Total Environ.*, 2017, **595**, 691–701.
6 S. Nawaz, Y. Khan, S. Khalid, M. A. Malik and M. Siddiq, *RSC Adv.*, 2023, **13**, 28785–28797.

7 W. T. Cui, L. Cao, J. H. Liu, Z. H. Ren, B. Zhao and S. Z. Dou, *Sci. Total Environ.*, 2020, **718**, 137234.
8 H. Wang, Q. Sui, J. Zhao, X. M. Sun, L. Zhu, B. J. Chen, K. M. Qu and B. Xia, *J. Hazard. Mater.*, 2023, **453**, 131361.
9 M. C. Passarelli, I. Riba, A. Cesar, F. Serrano-Bernando and T. A. DelValls, *Sci. Total Environ.*, 2017, **595**, 759–768.
10 S. J. Lin, *Nat. Commun.*, 2023, **14**, 2699.
11 A. Gallo, M. C. Esposito, A. Cuccaro, M. C. Buia, A. Tarallo, V. Monfrecola, E. Tosti and R. Boni, *Environ. Pollut.*, 2020, **265**, 115063.
12 T. Fujii, F. Moynier, M. Abe, K. Nemoto and F. Albarède, *Geochim. Cosmochim. Acta*, 2013, **110**, 29–44.
13 K. J. Powell, P. L. Brown, R. H. Byrne, T. Gajda, G. Hefter, S. Sjöberg and H. Wanner, *Pure Appl. Chem.*, 2007, **79**, 895–950.
14 M. Yabanlı, İ. Şener, A. Yozukmaz, S. Öner and H. H. Yapıcı, *Environ. Sci. Pollut. Res.*, 2021, **28**, 53171–53180.
15 J. Zheng, Q. Li and X. D. Zheng, *Sci. Total Environ.*, 2023, **891**, 164473.
16 N. Adimalla and H. K. Wang, *Arabian J. Geosci.*, 2018, **11**, 684.
17 Y. X. Yang, Z. P. Zhong, Ji. F. Li, H. R. Du, Q. Li, X. Zheng, R. Z. Qi, S. Zhang, P. K. Ren and Z. Y. Li, *Appl. Energy*, 2023, **351**, 121829.
18 N. A. A. Qasem, R. H. Mohammed and D. U. Lawal, *npj Clean Water*, 2021, **4**, 36.
19 M. Zhai, B. Fu, Y. H. Zhai, W. J. Wang, A. Maroney, A. A. Keller, H. T. Wang and J. M. Chovelon, *Water Res.*, 2023, **236**, 119924.
20 M. Zheng, F. Ma, M. X. Liu, M. J. Li, Q. J. Yu, H. D. Zhu, H. L. Guo and H. M. Sun, *J. Cleaner Prod.*, 2023, **395**, 136387.
21 H. Awes, Z. Zaki, S. Abbas, H. Dessoukii, A. Zaher, S. A. A. Moaty, N. Shehata, A. Farghali and R. K. Mahmoud, *Environ. Sci. Pollut. Res.*, 2021, **28**, 47651–47667.
22 Y. Sun, B. Y. Peng, Y. Wang, X. J. Wang, S. Q. Xia and J. F. Zhao, *Chem. Eng. J.*, 2023, **464**, 142714.
23 Q. M. Truong, P. N. T. Ho, T. B. Nguyen, W. H. Chen, X. T. Bui, A. K. Patel, R. R. Singhania, C. W. Chen and C. D. Dong, *Bioresour. Technol.*, 2022, **361**, 127732.
24 N. J. Che, N. Liu, Y. H. Li, C. Li, Y. L. Liu and C. L. Li, *Biochar*, 2022, **4**, 65.
25 S. C. Kishore, R. Atchudan, S. Perumal, T. N. J. I. Edison, Y. R. Lee, A. K. Sundramoorthy, R. Vinodh and M. Alagan, *J. Nanostruct. Chem.*, 2023, **13**, 545–561.
26 J. M. Liu, S. R. Zhao, C. B. Wang, Y. D. Ma, L. H. He, B. Z. Liu and Z. H. Zhang, *J. Colloid Interface Sci.*, 2022, **608**, 1627–1637.
27 Y. C. Pang, S. Y. Zhang, L. M. Liu, J. Liang, Z. J. Sun, Y. K. Wang, C. H. Xiao, D. W. Ding and S. J. Ding, *J. Mater. Chem. A*, 2017, **5**, 17963–17972.
28 H. Chen, H. C. Jiang, X. P. Cao, Y. T. Zhang, X. J. Zhang and S. L. Qiao, *Mater. Chem. Phys.*, 2020, **252**, 123244.
29 L. Z. Chen, K. Wu, M. H. Zhang, N. S. Liu, C. X. Li, Ji. Z. Qin, Q. L. Zhao and Z. F. Ye, *Chem. Eng. J.*, 2023, **466**, 143082.
30 S. Q. Wen, H. Q. Wang, Q. Xin, E. Hu, Z. W. Lei, F. Hu and Q. L. Wang, *Carbohydr. Polym.*, 2023, **315**, 120970.
31 K. C. Huang, S. Q. Yang, X. H. Liu, C. Zhu, F. L. Qi, K. Wang, J. Q. Wang, Q. S. Wang, T. Wang and P. Y. Ma, *J. Cleaner Prod.*, 2023, **391**, 136174.
32 F. Bu, W. Huang, M. Xian, X. L. Zhang, F. B. Liang, X. C. Liu, X. Y. Sun and D. X. Feng, *J. Cleaner Prod.*, 2022, **336**, 130485.
33 Z. Peng, S. Luo, D. D. Zhao and J. Zhang, *J. Cleaner Prod.*, 2023, **385**, 135655.
34 J. Q. Ma, N. Z. F. Jia, H. X. Jin, S. J. Yao, K. F. Zhang, Y. Kai, W. L. Wu and Y. Z. Wen, *Sep. Purif. Technol.*, 2023, **317**, 123880.
35 K. D. Rasamani, F. Alimohammadi and Y. G. Sun, *Mater. Today*, 2017, **20**, 83–91.
36 C. Wang, H. W. Wang, C. X. Yang, B. K. Dang, C. C. Li and Q. F. Sun, *Carbon*, 2020, **168**, 624–632.
37 C. Senthil, S. Amutha, R. Gnanamuthu, K. Vediappan and C. W. Lee, *Appl. Surf. Sci.*, 2019, **491**, 180–186.
38 U. Ghani, N. Iqbal, J. H. Li, A. A. Aboalhassan, B. Y. Sun, B. W. Liu, F. Ullah, J. Zeb, M. Imtiaz, J. J. Gu and Q. L. Liu, *Electrochim. Acta*, 2022, **432**, 141130.
39 D. Z. Wang, X. Y. Zhang, S. Y. Bao, Z. T. Zhang, H. Fei and Z. Z. Wu, *J. Mater. Chem. A*, 2017, **5**, 2681–2688.
40 Q. M. Luo, L. Sun, Y. W. Zhao, C. Wang, H. Q. Xin, D. Y. Li and F. Ma, *J. Mater. Sci. Technol.*, 2023, **145**, 165–173.
41 J. F. Fang, W. B. You, C. Y. Xu, B. T. Yang, M. Wang, J. C. Zhang and R. C. Che, *Small*, 2023, **19**, 2205407.
42 S. Q. Huang, B. Gong, Y. X. Jin, P. H. L. Sit and J. C. H. Lam, *ACS Catal.*, 2022, **12**, 11340–11354.
43 X. Zhang, T. Ma, T. Fang, Y. Z. Gao, S. Gao, W. W. Wang and L. X. Liao, *J. Alloys Compd.*, 2020, **818**, 152821.
44 X. H. Pi, X. X. Sun, R. Q. Wang, C. L. Chen, S. B. Wu, F. R. Zhan, J. B. Zhong, Q. Wang and K. K. Ostrikov, *J. Colloid Interface Sci.*, 2023, **629**, 227–237.
45 J. H. Li, Y. Q. Zhang, Y. Y. Mao, Y. Y. Zhao, D. X. Kan, K. Zhu, S. L. Chou, X. T. Zhang, C. L. Zhu, J. Ren and Y. J. Chen, *Angew. Chem., Int. Ed.*, 2023, **34**, 202303056.
46 M. G. Shang, X. Q. Peng, J. Zhang, X. C. Liu, Z. P. Yuan, X. F. Zhao, S. J. Liu, S. M. Yu, X. B. Yi and S. Filatov, *ACS Appl. Mater. Interfaces*, 2023, **15**, 14634–14642.
47 L. Z. Chen, K. Wu, M. H. Zhang, N. S. Liu, C. X. Li, J. Z. Qin, Q. L. Zhao and Z. F. Ye, *Chem. Eng. J.*, 2023, **466**, 143082.
48 Z. K. Xiong, H. L. Zheng, Y. D. Hu, X. B. Hu, W. Ding, J. Y. Ma and Y. S. Li, *Sep. Purif. Technol.*, 2021, **277**, 119053.
49 Y. Y. Xie, X. Z. Yuan, Z. B. Wu, G. M. Zeng, L. B. Jiang, X. Peng and H. Li, *J. Colloid Interface Sci.*, 2019, **536**, 440–455.
50 Z. Li, Y. P. Li, Z. Fu, L. B. Lu, J. R. Cheng and Y. S. Fei, *J. Colloid Interface Sci.*, 2021, **594**, 141–149.
51 J. Liu, R. Y. Zhou, J. X. Yu, L. Guo, X. D. Li, C. Q. Xiao, H. B. Hou, R. Chi and G. Q. Feng, *J. Environ. Manage.*, 2022, **322**, 116157.
52 C. L. Zhou, X. Y. Wang, Y. W. Wang, X. Song, D. F. Fang and S. F. Ge, *J. Environ. Chem. Eng.*, 2021, **9**, 105240.
53 Y. Priastomo, H. R. Setiawan, Y. S. Kurniawan and K. Ohto, *J. Environ. Chem. Eng.*, 2020, **8**, 103971.
54 Q. Y. Wang, L. P. Li, L. C. Kong, G. Y. Cai, P. Wang, J. Zhang, W. Zuo and Y. Tian, *Sep. Purif. Technol.*, 2022, **293**, 121146.
55 Z. H. Lin, R. K. Wang, S. T. Tan, K. Zhang, Q. Yin, Z. H. Zhao and P. Gao, *J. Environ. Manage.*, 2023, **334**, 117503.

56 Y. Y. Zhao, H. X. Hu, L. C. Zhan, Z. J. Xue, K. K. YusefF and M. J. Wu, *J. Chem.*, 2020, **2020**, 13.
57 M. J. Han, X. Wei, R. Wang, J. Li, W. Sun and C. Y. Zhang, *Sep. Purif. Technol.*, 2024, **330**, 125209.
58 T. Wu, X. W. Chen, H. G. Zhang, M. Zhao, L. Huang, J. Yan, M. H. Su and X. J. Liu, *Sep. Purif. Technol.*, 2023, **304**, 122284.
59 J. M. Luo, K. X. Fu, M. Sun, K. Yin, D. Wang, X. Liu and J. C. Crittenden, *ACS Appl. Mater. Interfaces*, 2019, **11**, 38789–38797.